Bimetallic Nanoparticles

International Edition: DOI: 10.1002/anie.201806447
German Edition: DOI: 10.1002/ange.201806447

Kinetics of Lifetime Changes in Bimetallic Nanocatalysts Revealed by Quick X-ray Absorption Spectroscopy

Matthias Filez, Hilde Poelman, Evgeniy A. Redekop, Vladimir V. Galvita,* Konstantinos Alexopoulos, Maria Meledina, Ranjith K. Ramachandran, Jolien Dendooven, Christophe Detavernier, Gustaaf Van Tendeloo, Olga V. Safonova, Maarten Nachtegaal, Bert M. Weckhuysen, and Guy B. Marin*

Abstract: *Alloyed metal nanocatalysts are of environmental and economic importance in a plethora of chemical technologies. During the catalyst lifetime, supported alloy nanoparticles undergo dynamic changes which are well-recognized but still poorly understood. High-temperature O_2–H_2 redox cycling was applied to mimic the lifetime changes in model $Pt_{13}In_9$ nanocatalysts, while monitoring the induced changes by in situ quick X-ray absorption spectroscopy with one-second resolution. The different reaction steps involved in repeated $Pt_{13}In_9$ segregation-alloying are identified and kinetically characterized at the single-cycle level. Over longer time scales, sintering phenomena are substantiated and the intra-particle structure is revealed throughout the catalyst lifetime. The in situ time-resolved observation of the dynamic habits of alloyed nanoparticles and their kinetic description can impact catalysis and other fields involving (bi)metallic nanoalloys.*

Bimetallic catalysts can exhibit drastically increased selectivity, activity, and stability compared to their monometallic siblings owing to an interplay of electronic and geometric effects. They are the workhorses in widespread technologies, such as car exhaust converters,[1] and fuel cells,[2] and have acquired a pivotal role in chemical industry. Within the library of bimetallic catalysts, archetypal Pt-based catalysts promote a vast array of reactions,[3] such as NO_x reduction[1] (e.g. Pt-Rh) to alkane dehydrogenation[4–6] (e.g. Pt-In). In reaction, these catalysts operate at high temperature under rapidly changing reductive and oxidative environments.[7,8] For example, dehydrogenation catalysts require cyclic O_2-H_2 redox treatments to regenerate (O_2) and reactivate (H_2) Pt-In nanoalloys after coking in high-temperature alkane flows.[9–11]

Whilst catalysts were originally assumed to be static substances, intense research in the past decades has witnessed that (bi)metal catalysts are dynamically changing nanomaterials under reaction conditions.[12] During the catalyst lifetime, multiple atomic scale processes shape the working state of the catalyst and thereby influence its performance. It goes without saying that understanding these processes and detailing their kinetics is of crucial importance to control their occurrence and thus the catalyst performance. To this aim, techniques which provide high time resolution, but do not require long range order and can be applied in situ, are crucial for interrogating the kinetic behavior of (often disordered) bimetallic nanocatalysts under operating conditions. For example, in situ, dispersive and quick X-ray absorption spectroscopy (XAS) have established a role of utmost importance in uncovering the motifs of (bi)metallic nanoparticle restructuring.[13–18]

[*] Dr. M. Filez, Dr. H. Poelman, Dr. E. A. Redekop, Dr. V. V. Galvita, Dr. K. Alexopoulos, Prof. G. B. Marin
Laboratory for Chemical Technology, Ghent University
Technologiepark 914, 9052 Ghent (Belgium)
E-mail: m.filez@uu.nl
vladimir.galvita@ugent.be

Dr. M. Meledina, Prof. G. Van Tendeloo
Electron microscopy for materials science, University of Antwerp
Groenenborgerlaan 171, 2020 Antwerp (Belgium)

Dr. R. K. Ramachandran, Dr. J. Dendooven, Prof. C. Detavernier
Conformal Coatings of Nanomaterials group, Ghent University
Krijgslaan 281/S1, 9000 Ghent (Belgium)

Dr. O. V. Safonova, Dr. M. Nachtegaal
Paul Scherrer Institute
5232 Villigen PSI (Switzerland)

Prof. B. M. Weckhuysen
Inorganic Chemistry and Catalysis group, Utrecht University
Universiteitsweg 99, 3584CG Utrecht (The Netherlands)

Dr. M. Filez
Current address: Inorganic Chemistry and Catalysis group, Utrecht University
Universiteitsweg 99, 3584CG Utrecht (The Netherlands)

Dr. E. A. Redekop
Current address: Centre for Materials Science and Nanotechnology, University of Oslo
P.O box 1126 Blindern, 0318 Oslo (Norway)

Dr. K. Alexopoulos
Current address: Department of Chemical & Biomolecular Engineering, University of Delaware
Newark, DE 19716 (USA)

Dr. M. Meledina
Current address: Central Facility for Electron Microscopy, RWTH Aachen
Ahornstraße 55, 52074 Aachen (Germany)

Supporting information and the ORCID identification number(s) for the author(s) of this article can be found under: https://doi.org/10.1002/anie.201806447.

Herein, we probe the dynamic lifetime changes in a $Pt_{13}In_9$ model nanocatalyst induced by high-temperature O_2–H_2 redox cycling with quick X-ray absorption spectroscopy (QXAS). Such Pt-In catalysts show great promise for alkane dehydrogenation, hydroconversion of bio-based oxygenates, and as direct methanol and ethanol fuel cells.[3] Additionally, efforts have been undertaken recently by our groups[19–22] and others[23,24] to understand their formation and control their intermetallic composition. To monitor the kinetic habits of these catalysts in situ with high time resolution, QXAS spectra are recorded at the Pt L_3-edge with one second time resolution (Figure 1a). While pioneering in situ QXAS studies on the formation and working state of nanocatalysts are available,[7,25–30] the quantitative extraction of kinetic data and the construction of a full reaction mechanism has, to our best knowledge, not been reported for

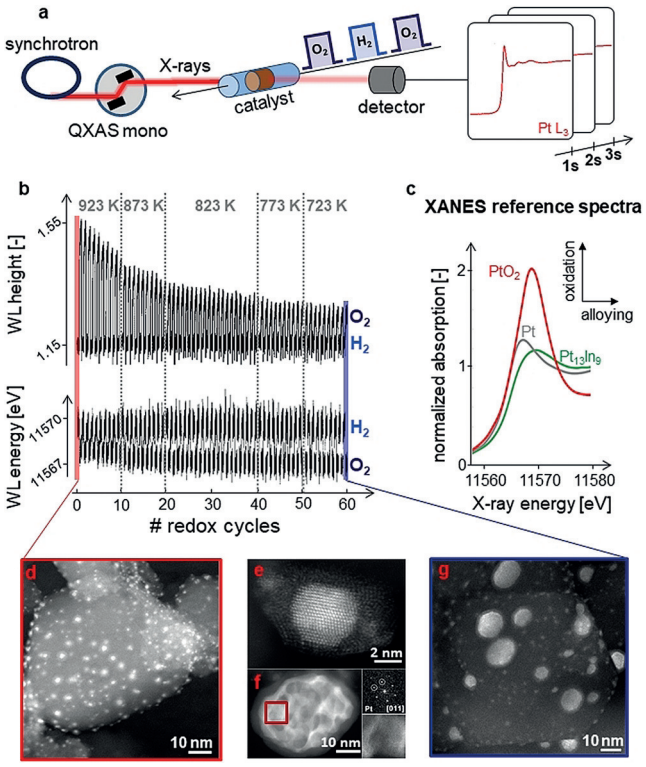

Figure 1. a) Synchrotron source producing an X-ray beam by a quick-scanning channel-cut monochromator; the X-ray beam irradiates the catalyst bed, contained in a capillary by which cyclic H_2-O_2 pulses are flown to induce structural changes in the Pt-In nanocatalyst. The X-ray absorption spectrum is measured by the X-ray detector with 1 s time resolution. b) Pt L_3-edge XANES white line (WL) analysis yielding the (top) WL height in terms of normalized absorption and (bottom) WL energy (at the WL maximum) in eV, as a function of the number of H_2-O_2 redox cycles. The experiments are performed at variable temperature, ranging from 923 K down to 723 K. c) XANES reference spectra of PtO_2, Pt and $Pt_{13}In_9$. HAADF-STEM images of Pt-In nanoparticle catalysts after d, e) 1 and f, g) 60 redox cycles. e) HAADF-STEM of Pt-In nanoparticle after the first H_2-O_2 cycle, that is, after re-oxidation and alloy segregation, showing a bright contrast Pt core surrounded by a dark contrast In oxide shell. f) HAADF-STEM image of sintered nanoparticles after 60 redox cycles in oxidized (alloy segregated) state, showing Pt nanoworm network formation, surrounded by In oxide, together with magnified region (red square) and corresponding FFT.

(bi)metallic nanoparticles. For this work, phase-pure Pt-In alloys were fabricated by atomic layer deposition[19] (ALD) and their XAS spectra measured to benchmark the QXAS data in their Pt-In composition during O_2-H_2 cycling. This allows to probe Pt-In nanoalloy-segregation dynamics on a quantitative level and to extract kinetic information.

The white line (WL) height and energy position of the X-ray absorption near edge structure (XANES) spectra are used to probe the state of Pt in situ during repetitive H_2-O_2 redox cycling (Figure 1b, Supporting Information, section S4). Reference XANES spectra show that 1) Pt oxidation mainly results in an increase in the WL height (PtO_2), while 2) Pt alloying towards $Pt_{13}In_9$ primarily results in a blue shift of the WL energy (Figure 1c; Supporting Information, sections S2,4). The WL height reversibly alternates from low to high values, respectively during H_2 and O_2 pulses, and vice versa for the WL energy. This suggests that Pt reversibly undergoes PtO_x reduction and Pt-In alloying (H_2), followed by Pt-In alloy segregation and re-oxidation into PtO_x (O_2).

The WL height and energy position remain constant at the end of each H_2 pulse, implying that the alloy composition is stable for at least 60 H_2-O_2 cycles. In contrast, the WL height strongly decreases in O_2 with increasing number of redox cycles as a result of Pt nanoparticle (NP) sintering. HAADF-STEM confirms that initially well-dispersed NPs (ca. 2 nm, Figure 1d) sinter into larger ones (ca. 10 nm, Figure 1g), steered by H_2-O_2 cycling. A magnified view of a small NP obtained after one H_2-O_2 redox cycle, that is, in oxidized state, shows that the NP is composed of a metallic Pt core, surrounded by an In_2O_3 crust (Figure 1e). Large NPs after 60 H_2-O_2 redox cycles reveal a nanocomposite consisting of a Pt nanoworm network surrounded by In_2O_3, as confirmed by EDX (Supporting Information, section S7) and fast Fourier transformed (FFT) analysis showing face centered cubic (fcc) Pt (Figure 1f). Such nanocomposite structure suggests that nanoalloys decompose spinodally, as caused by kinetically rapid segregation.

The dynamic changes of Pt are now studied at the single cycle level. Figure 2a displays the Pt L_3-edge wavelet transformed (WT) quick extended X-ray absorption fine structure (EXAFS) magnitude at specific points in redox cycle 21.[20] At the end of the H_2 pulse, the WT-EXAFS magnitude shows both Pt and In around Pt and mix to form a Pt-In alloy (Figure 2a,1; 116 s in H_2). In the middle of the O_2 pulse both Pt and O are observed, but no In, indicating that the Pt-In alloy has decomposed by segregation (Figure 2a,3; 60 s in O_2). This results in phase-pure Pt with some degree of surface oxidation (suggested by XANES). After the start in H_2, only In is visible in WT-EXAFS, while Pt is barely observed (Figure 2a,5; 4 s in H_2), showing that the Pt-In alloy is still evolving to a local equilibrium state and might be disordered. At the very start of the O_2 and H_2 pulses, WT-EXAFS plots show intermediate states with combined contributions from Pt, In and O (Figure 2a,2 and 2.a,4; 0 s).

The XANES WL height and energy position in Figure 2b uncover the kinetics of the processes occurring within one H_2-O_2 redox cycle. During the O_2 pulse, the decomposition of the initial Pt-In nanoalloy into fcc Pt and In (oxide) is rapid (WL energy shift), clarifying the spinodal nanostructure observed

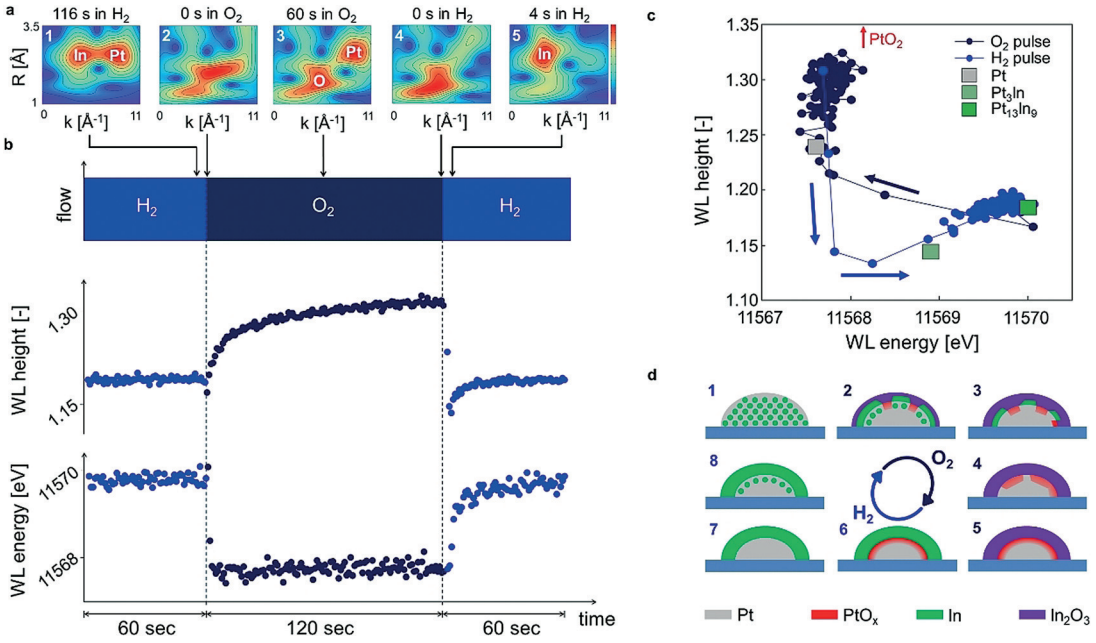

Figure 2. a) Pt L_3-edge wavelet transformed (WT) quick EXAFS magnitude maps at five points in time (1–5) at the single cycle level after 21 H_2-O_2 redox cycles. The plots reveal the element type (k-axis) and position (R-axis) of neighbors around Pt, namely In, O or Pt. The color bar represents the normalized intensity (0–1) of the WT QEXAFS magnitude. b) The WL height and energy versus time within the 21st redox cycle. Light blue (navy blue) corresponds to H_2 (O_2) gas environment resp. in panels (b–d). c) The transient evolution of the WL maximum during H_2-O_2 redox cycle 21 at 893 K, evolving from $Pt_{13}In_9$ to a segregated PtO_x state (O_2) and back to $Pt_{13}In_9$ (H_2) via the Pt_3In intermediate. The WL positions of Pt, Pt_3In and $Pt_{13}In_9$ references are shown in the squares. d) Mechanism of reversible Pt-In segregation, Pt oxidation and Pt-In re-alloying at the single H_2-O_2 redox level: (2–5) simultaneous $Pt_{13}In_9$ segregation, Pt surface oxidation, (5–8,1) consecutive Pt reduction and Pt-In alloying.

by HAADF-STEM for Pt-In_2O_3 nanonetworks. Simultaneous to alloy segregation, a slower Pt oxidation process takes place at the Pt surface, which is not entirely stabilized even within the 120 s O_2 pulse (WL height). In contrast to Pt oxidation, Pt reduction at the start of the H_2 pulse is completed in 2 s. Thereafter, Pt-In alloying takes place, which in contrast to Pt oxidation stabilizes within the H_2 period.

Figure 2c shows the evolution of the WL in time for both the O_2 (navy blue) and H_2 (light blue) pulses. Additionally, the white line positions of ALD-derived phase-pure Pt, Pt_3In, and $Pt_{13}In_9$ are depicted (Supporting Information, S2). Notably, the final WL position in H_2 matches to a stoichiometric $Pt_{13}In_9$ alloy. There is a marked difference between the alloy formation and decomposition process. Pt-In alloy formation sets in after full reduction of PtO_x into Pt by a further drop in WL height (consecutive processes). The evolution from fcc Pt to $Pt_{13}In_9$ presumably occurs via the fcc Pt_3In intermediate, established by the gradual but rapid incorporation of In into fcc Pt. Thereafter, the further uptake of In transforms Pt_3In (75% Pt) into intermetallic $Pt_{13}In_9$ (59% Pt), which is kinetically slower. In contrast, Pt-In alloy decomposition occurs simultaneously with Pt surface oxidation to PtO_x (parallel processes). Instead of evolving via Pt_3In and Pt references towards PtO_x, the WL height shows a monotonic, upward trend that is intermediate to the phase-pure reference positions. Figure 2d illustrates the full redox process.

To perform a full kinetic analysis, the 60 H_2-O_2 redox cycles are executed at temperatures ranging from 923 K down to 723 K in steps of 50 K for each 10 cycles, except for 823 K which is kept for 20 cycles (Figure 1b). The WL height and energy are used for kinetic modeling of the degree of Pt oxidation and Pt-In alloying over time, respectively. First, WL-time data are averaged over all cycles at a given temperature to reduce noise (Supporting Information, section S6). Next, the WL time evolution is modelled by a zero- and/or first-order rate law. This yields rate coefficients for each temperature, from which Arrhenius plots are constructed and apparent activation energies E_a are estimated for the reduction/alloying and segregation/ oxidation processes (Figure 3a,b). Additionally, 1) an estimated content of Pt in Pt-In alloys during segregation and alloying (resp. Figure 3c,d), and 2) the extent of Pt oxidation during H_2/O_2 oxidation/reduction (resp. Figure 3e,f, S6) are extracted.

During the O_2 pulse, the majority of In dealloys by segregating out of the $Pt_{13}In_9$ alloy in 5 seconds by a first-order process (Figure 3c, green). The much slower Pt surface oxidation can only be modelled by combining a first-order rate law (Figure 3e, red) with a zero-order reaction with constant rate (Figure 3e, blue). The latter leads to a continuous increase in Pt oxidation state throughout the entire O_2 pulse, and is presumably caused by diffusion controlled redispersion of Pt into smaller NPs after spinodal decomposition. The first- order processes, namely $Pt_{13}In_9$ dealloying and initial Pt surface oxidation, show strong temperature dependence. Their Arrhenius plots (Figure 3a, red) exhibit linear correlations with relatively high slopes, yielding apparent activation energies of 67 ± 1 kJ mol^{-1} for $Pt_{13}In_9$

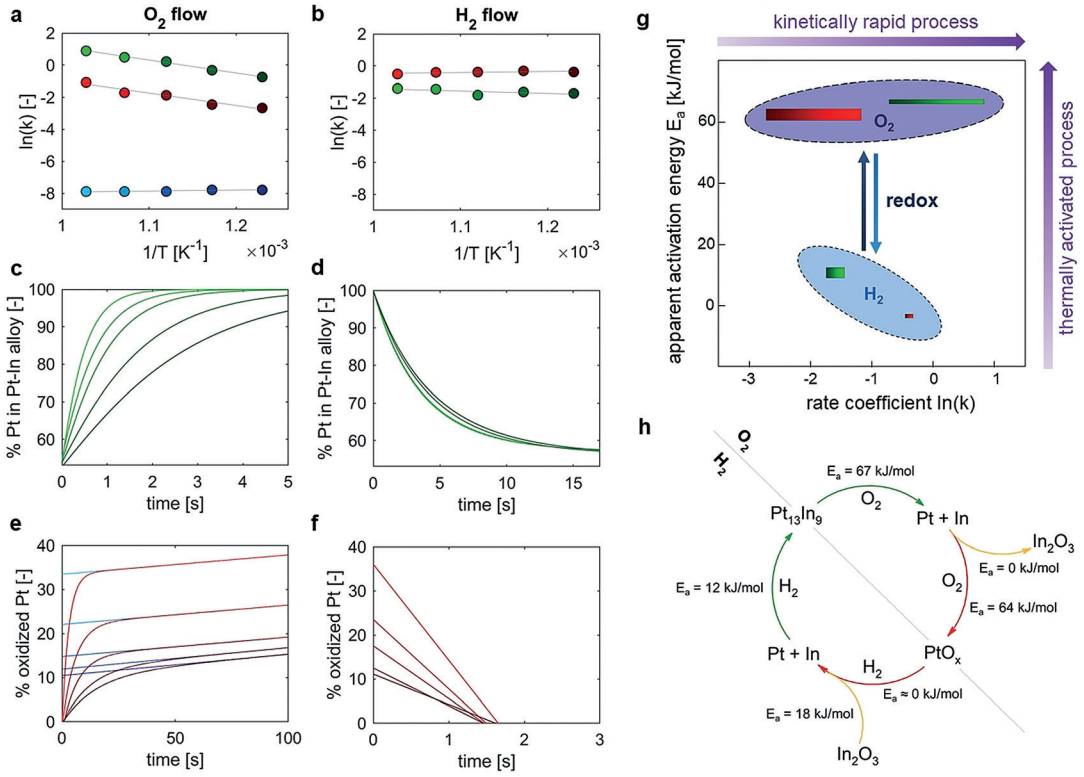

Figure 3. a) The Arrhenius plots for (green) Pt-In segregation, (red) Pt surface oxidation, and (blue) Pt diffusion-controlled oxidation process; c) green, and e) red and blue, respectively, are their modeled curves to WL XANES data (darker colors correspond to lower temperatures). b) Arrhenius plot for (green) Pt-In alloying and (red) Pt reduction, and their concomitant fits to the WL XANES during d) alloying (modeled) and f) reduction (Supporting Information, section S6) as a function of time. g) E_a versus ln(k) for (red, top) Pt oxidation, (green, top) Pt-In segregation in O_2 and (green, bottom) Pt-In alloying and (red, bottom) PtO_x reduction in H_2. The rectangle width represents the range that ln(k) varies across the measured temperature range, while its height is the 66% confidence interval of E_a. h) reaction mechanism derived from Arrhenius plots in (a) and (b). In_2O_3 activation energies are obtained from redox data collected at different temperature at the In K-edge as further detailed at the end of Suporting Information, section S6.

dealloying and 64 ± 4 kJ mol^{-1} for initial Pt surface oxidation. The zero-order process approaches a zero activation energy (Supporting Information, section S6). Notably, the order of magnitude of the rate coefficients of Pt surface oxidation accords with an earlier study,[31] assessing Pt NP oxidation only.

During the H_2 pulse, surface oxidized Pt is fully reduced to metallic Pt with a high rate (in 1.5 s; Figure 3 f). The activation energy retrieved in a qualitative way from the Arrhenius plot approaches zero (for more information see Supporting Information, section S6,and Figure 3 b). Similar to $Pt_{13}In_9$ segregation, Pt-In alloying is described by a first-order rate law with now an activation energy of only 12 ± 3 kJ mol^{-1} (Figure 3 d).

Figure 3 g and h present an overview of E_a-ln(k) space and a reaction mechanism for the $Pt_{13}In_9$-PtO_x-$Pt_{13}In_9$ redox process. The E_a–ln(k) plot shows that the apparent activation energies for $Pt_{13}In_9$ segregation and Pt oxidation in O_2 are significantly higher compared to PtO_x reduction and Pt-In alloying in H_2, and therefore require thermal activation. While Pt surface oxidation (Figure 3 g, O_2-red) is the rate-determining step in O_2, In_2O_3 reduction (Supporting Information, section S6, last page) together with Pt-In alloying (Figure 3 g, H_2-green) are kinetically the slowest processes in H_2. In O_2 flow, the stability of In_2O_3/PtO_x drives the segregation of $Pt_{13}In_9$ to segregated In/Pt, while the driving force for In_2O_3/PtO_x reduction and alloying in H_2 is the stability of the $Pt_{13}In_9$ nanoalloy (Figure 3 h).

In summary, we have demonstrated that kinetic modeling of in situ quick X-ray absorption spectroscopy data can result in the unrivaled identification of the reaction mechanism describing the dynamic restructuring of nanoparticles. The approach allowed to elucidate the steps involved in alloying-segregation of $Pt_{13}In_9$ alloys into In_2O_3/PtO_x nanocomposites during high-temperature H_2–O_2 redox cycling. In O_2, $Pt_{13}In_9$ decomposition and Pt surface oxidation are discerned as simultaneous processes exhibiting high activation energy in which Pt oxidation is rate-determining. In contrast, the reverse processes in H_2 drive the equilibrium state from In_2O_3/PtO_x back to $Pt_{13}In_9$ through In_2O_3 and PtO_x reduction followed by Pt-In alloying, both exhibiting low apparent activation energies. This QXAS approach can be applied to a wide variety of (bi)metallic nanocatalysts and by extension to any field studying dynamic changes in bimetallic nanoparticles and nanomaterials.

Acknowledgements

M.F. acknowledges a European Union's Horizon 2020 research and innovation program under the Marie Sklodowska-Curie grant agreement (No. 748563). E.A.R acknowledges the Marie Curie International Incoming Fellowship granted by the European Commission (No. 301703). This work was supported by the Fund for Scientific Research Flanders (G.0209.11), the "Long Term Structural Methusalem Funding by the Flemish Government". The research leading to these results has received funding from the European Community's Seventh Framework Programme (FP7/2007–2013) under grant agreement No. 312284 (CALIPSO). We thanks the Swiss Light Source for providing beamtime at the SuperXAS beamline.

Conflict of interest

The authors declare no conflict of interest.

Keywords: alloying segregation · bimetallic nanoparticles · in situ time-resolved X-ray absorption spectroscopy · kinetics · oxidation–reduction

How to cite: *Angew. Chem. Int. Ed.* **2018**, *57*, 12430–12434
Angew. Chem. **2018**, *130*, 12610–12614

[1] P. Granger, V. I. Parvulescu, *Chem. Rev.* **2011**, *111*, 3155.
[2] A. Kulkarni, S. Siahrostami, A. Patel, J. K. Nørskov, *Chem. Rev.* **2018**, *118*, 2302.
[3] W. Yu, M. D. Porosoff, J. G. Chen, *Chem. Rev.* **2012**, *112*, 5780–5817.
[4] J. J. H. B. Sattler, J. Ruiz-Martinez, E. Santillan-Jimenez, B. M. Weckhuysen, *Chem. Rev.* **2014**, *114*, 10613.
[5] H. Xiong, S. Lin, J. Goetze, P. Pletcher, H. Guo, L. Kovarik, K. Artyushkova, B. M. Weckhuysen, A. K. Datye, *Angew. Chem. Int. Ed.* **2017**, *56*, 8986; *Angew. Chem.* **2017**, *129*, 9114.
[6] L.-L. Shen, K. Xia, W.-Z. Lang, L.-F. Chu, X. Yan, Y.-J. Guo, *Chem. Eng. J.* **2017**, *324*, 336.
[7] Y. Nagai, K. Dohmae, Y. Ikeda, N. Takagi, T. Tanabe, N. Hara, G. Guilera, S. Pascarelli, M. A. Newton, O. Kuno, et al., *Angew. Chem. Int. Ed.* **2008**, *47*, 9303; *Angew. Chem.* **2008**, *120*, 9443.
[8] G. Siddiqi, P. Sun, V. Galvita, A. T. Bell, *J. Catal.* **2010**, *274*, 200.
[9] A. Iglesias-Juez, A. M. Beale, K. Maaijen, T. C. Weng, P. Glatzel, B. M. Weckhuysen, *J. Catal.* **2010**, *276*, 268.
[10] E. A. Redekop, V. V. Galvita, H. Poelman, V. Bliznuk, C. Detavernier, G. B. Marin, *ACS Catal.* **2014**, *4*, 1812.
[11] J. Im, M. Choi, *ACS Catal.* **2016**, *6*, 2819.
[12] R. Schlögl, *Angew. Chem. Int. Ed.* **2015**, *54*, 3465; *Angew. Chem.* **2015**, *127*, 3531.
[13] A. E. Russell, A. Rose, *Chem. Rev.* **2004**, *104*, 4613.
[14] C. Roth, N. Benker, T. Buhrmester, M. Mazurek, M. Loster, H. Fuess, D. C. Koningsberger, D. E. Ramaker, *J. Am. Chem. Soc.* **2005**, *127*, 14607.
[15] D. Liu, Y. Li, M. Kottwitz, B. Yan, S. Yao, A. Gamalski, D. Grolimund, O. V. Safonova, M. Nachtegaal, J. G. Chen, et al., *ACS Catal.* **2018**, *8*, 4120.
[16] J. A. Rodriguez, J. C. Hanson, A. I. Frenkel, J. Y. Kim, M. Pérez, *J. Am. Chem. Soc.* **2002**, *124*, 346.
[17] I. Böttger, T. Schedel-Niedrig, O. Timpe, R. Gottschall, M. Hävecker, T. Ressler, R. Schlögl, *Chem. Eur. J.* **2000**, *6*, 1870.
[18] A. Suzuki, Y. Inada, A. Yamaguchi, T. Chihara, M. Yuasa, M. Nomura, Y. Iwasawa, *Angew. Chem. Int. Ed.* **2003**, *42*, 4795; *Angew. Chem.* **2003**, *115*, 4943.
[19] R. K. Ramachandran, J. Dendooven, M. Filez, V. V. Galvita, H. Poelman, E. Solano, M. M. Minjauw, K. Devloo-Casier, E. Fonda, D. Hermida-Merino, et al., *ACS Nano* **2016**, *10*, 8770.
[20] M. Filez, E. A. Redekop, H. Poelman, V. V. Galvita, G. B. Marin, *Anal. Chem.* **2015**, *87*, 3520.
[21] M. Filez, E. A. Redekop, V. V. Galvita, H. Poelman, M. Meledina, S. Turner, G. Van Tendeloo, A. T. Bell, G. B. Marin, *Phys. Chem. Chem. Phys.* **2016**, *18*, 3234.
[22] M. Filez, E. A. Redekop, H. Poelman, V. V. Galvita, M. Meledina, S. Turner, G. V. Tendeloo, C. Detavernier, G. B. Marin, *Catal. Sci. Technol.* **2016**, *6*, 1863.
[23] E. C. Wegener, Z. Wu, H.-T. Tseng, J. R. Gallagher, Y. Ren, R. E. Diaz, F. H. Ribeiro, J. T. Miller, *Catal. Today* **2018**, *299*, 146.
[24] P. Sun, G. Siddiqi, W. C. Vining, M. Chi, A. T. Bell, *J. Catal.* **2011**, *282*, 165.
[25] S. Reimann, J. Stötzel, R. Frahm, W. Kleist, J.-D. Grunwaldt, A. Baiker, *J. Am. Chem. Soc.* **2011**, *133*, 3921.
[26] J.-D. Grunwaldt, A. M. Molenbroek, N.-Y. Topsøe, H. Topsøe, B. S. Clausen, *J. Catal.* **2000**, *194*, 452.
[27] M. A. Newton, C. Belver-Coldeira, A. Martínez-Arias, M. Fernández-García, *Nat. Mater.* **2007**, *6*, 528.
[28] M. A. Newton, W. van Beek, *Chem. Soc. Rev.* **2010**, *39*, 4845.
[29] J. Singh, E. M. C. Alayon, M. Tromp, O. V. Safonova, P. Glatzel, M. Nachtegaal, R. Frahm, J. A. van Bokhoven, *Angew. Chem. Int. Ed.* **2008**, *47*, 9260; *Angew. Chem.* **2008**, *120*, 9400.
[30] R. Kopelent, J. A. van Bokhoven, J. Szlachetko, J. Edebeli, C. Paun, M. Nachtegaal, O. V. Safonova, *Angew. Chem. Int. Ed.* **2015**, *54*, 8728; *Angew. Chem.* **2015**, *127*, 8852.
[31] Y. Uemura, Y. Inada, K. K. Bando, T. Sasaki, N. Kamiuchi, K. Eguchi, A. Yagishita, M. Nomura, M. Tada, Y. Iwasawa, *Phys. Chem. Chem. Phys.* **2011**, *13*, 15833.

Manuscript received: June 5, 2018
Revised manuscript received: July 12, 2018
Accepted manuscript online: August 1, 2018
Version of record online: August 28, 2018

